EARTHARXIV PREPRINT

Title:

Comprehensive Inventory of Coseismic Landslides Triggered by the 2023 Kahramanmaraş Earthquakes, Türkiye

Authors:

Abdüssamet Yılmaz[1], Hakan Tanyaş[2], Furkan Karabacak[1], Mehmet Lütfi Süzen[3], Tolga Görüm[1]

Affiliations:

[1]Eurasia Institute of Earth Sciences, Istanbul Technical University, Istanbul, Türkiye

[2]University of Twente, Faculty of Geo-Information Science and Earth Observation (ITC), Enschede, the Netherlands

[3]Middle East Technical University, Geological Engineering Department, Ankara, Türkiye

Corresponding authors:

Abdüssamet Yılmaz and Hakan Tanyaş

Email addresses and ORCID:

Abdüssamet Yılmaz: yilmazabd19@itu.edu.tr & https://orcid.org/0000-0002-8707-8649

Hakan Tanyaş: h.tanyas@utwente.nl & https://orcid.org/0000-0002-0609-2140

Furkan Karabacak: karabacak22@itu.edu.tr & https://orcid.org/0000-0001-5838-3196

Mehmet Lütfi Süzen: suzen@metu.edu.tr & https://orcid.org/0000-0003-0865-2022

Tolga Görüm: tgorum@itu.edu.tr & https://orcid.org/0000-0001-9407-7946

This manuscript is a non-peer-reviewed preprint submitted to EarthArXiv.

This manuscript is currently under review at Scientific Data.

Version:

Version 1

March 19, 2026

Abstract

We provide two geospatial inventories covering ~80,000 km² in southern Türkiye for the 6 February 2023 Kahramanmaraş earthquake sequence: (i) a coseismic landslide polygon inventory including 20,270 landslides and (ii) a pre-earthquake geomorphic inventory of pre-existing slope instability including 4,495 landslide polygons. Coseismic landslides were mapped by systematic expert visual interpretation of high-resolution optical pre- and post-event imagery, primarily 0.3 m post-event aerial photographs acquired by the Turkish General Directorate of Mapping. The pre-earthquake inventory was compiled from 5 m DEM-based Red Relief Image Maps. Coseismic landslides were digitized as full-footprint polygons and attributed by movement type (avalanche, slide, fall, flow, lateral spread, complex) and material (earth, debris, rock, rock–debris). The datasets are released to support event-based landslide analyses, model development and benchmarking, cross-event comparison, and future updates or extensions.

Background & Summary

Landslides in mountainous regions are commonly triggered by earthquakes[1,2], rainfall[3,4], snowmelt[5,6], and a variety of anthropogenic disturbances[7,8]. Regardless of the trigger, landslides have been documented either as individual occurrences or as events when a group of landslides is triggered by the same event that occurred at the same time or within a time window[9,10].

Over the last few decades, the production and public release of event-scale inventories have accelerated, particularly for earthquake-induced landslides[11]. These inventories provided a valuable source for various research directions including landscape evolution[12,13], hazard assessment[14,15].

From a global perspective, earthquake-induced landslide event inventories appear to be the most systematically stored and shared datasets compared to their counterparts associated with any other trigger[16,17]. One of the most systematically curated and openly shared collection of landslide event inventories is the one hosted by the U.S. Geological Survey (USGS) ScienceBase community, which provides a centralized repository of earthquake-triggered ground-failure inventories[18]. As of July 2025, this repository contains 62 digital landslide event inventories for 49 earthquakes.

From a global perspective, earthquake-induced landslide event inventories appear to be the most systematically stored and shared datasets compared to their counterparts associated with any other trigger[18]. To assess the quality and completeness, the most essential evaluation is done based on whether a given study area with a known areal extent was systematically surveyed using high temporal and spatial resolution datasets to map the majority of coseismic landslides[19]. In addition to this, some extra information on landslide source and run out areas as well as types labelled based on internationally valid classification systems is considered as preferable features contributing to the quality and completeness of an inventory[17].

However, in practice providing all this information is rarely the case in earthquake-induced landslide inventories. Despite all technical improvements including automated landslide detection algorithms[20,21] and/or freely accessible earth observatory datasets such as Sentinel-1, Sentinel-2 offering a relatively high temporal resolution (~10-20m), and large spatial coverage, especially for the large events where at least ten thousand of landslides were triggered, there are limited inventories providing such details. For instance, the 2004 Mw 6.6 Mid-Niigata, Japan inventory contains more than 10,000 landslides with source and deposit areas delineated separately[22]. The same is also valid for the inventory generated for the 2015 Mw 7.8 Gorkha, Nepal earthquake where more than 24,000 landslides were mapped[23].

Compared to mapping landslide source and runout areas separately, labelling landslide types in such a big event, on the other hand, is yet to be done to our best knowledge[17,18]. In this context, we can refer to some other inventories where landslide types in addition to source and runouts, were labelled for a relatively limited number of landslides (i.e., <5,000): e.g, the inventories created for the 2004 Mw 6.6 Mid-Niigata, Japan[24], the 2007 Mw 6.2 Aysén Fjord, Chile[25], the 2008 Mw 6.9 Iwate-Miyagi Nairiku[26] or the 2011 Mw 9.1 Eastern Honshu, Japan[27] earthquakes.

In addition to the event inventory specific quality and completeness measures mentioned above, in some cases, coseismic landslide inventories are temporarily expanded in post-seismic periods through multi-temporal inventories[28–30]. Such datasets contribute to the quality and completeness of landslide observations regarding to an earthquake-affected area as landslides do not occur in a completely intendent manner from each other temporarily[31]. However, it is much rarer to expand a coseismic landslide inventories backward in time and enrich the quality and completeness of landslide observations by mapping pre-seismic landslide mapping[32].

Study area

The research area covers the region strongly affected by the 6 February 2023 earthquake doublet in southeastern Türkiye (Fig. 1). This region is traversed by the East Anatolian Fault (EAF), a major intracontinental left-lateral strike-slip system that accommodates the relative motion between the Anatolian and Arabian plates[33–35]. The EAF extends from the Karlıova triple junction in the northeast, where it merges with the North Anatolian Fault, to the Iskenderun Gulf in the Mediterranean region. The fault zone spans approximately 550–700 km and consists of more than fifteen mapped fault segments[36,37]. Slip rates along the EAF decrease from roughly 10 mm per year in the northern part to about 4–5 mm per year in the southern section[35,38].

Two major earthquakes occurred on 6 February 2023 within this fault system. The first mainshock, with a moment magnitude (M_w) of 7.8, originated near Pazarcık and was followed about nine hours later by a M_w 7.5 event near Ekinözü[39,40]. The combined rupture propagated along several EAF segments and adjacent structures, producing surface breaks approximately 310 km long for the first event and 140–170 km for the second[41]. Maximum horizontal displacements reached up to 10 m along parts of the East Anatolian and Sürgü faults[42]. Geodetic observations from InSAR and GPS revealed strong spatial variations in slip distribution and locking depth, indicating a heterogeneous rupture pattern[43]. Modelling and seismological studies identified episodes of supershear propagation and cascading rupture involving multiple fault segments[44–46].

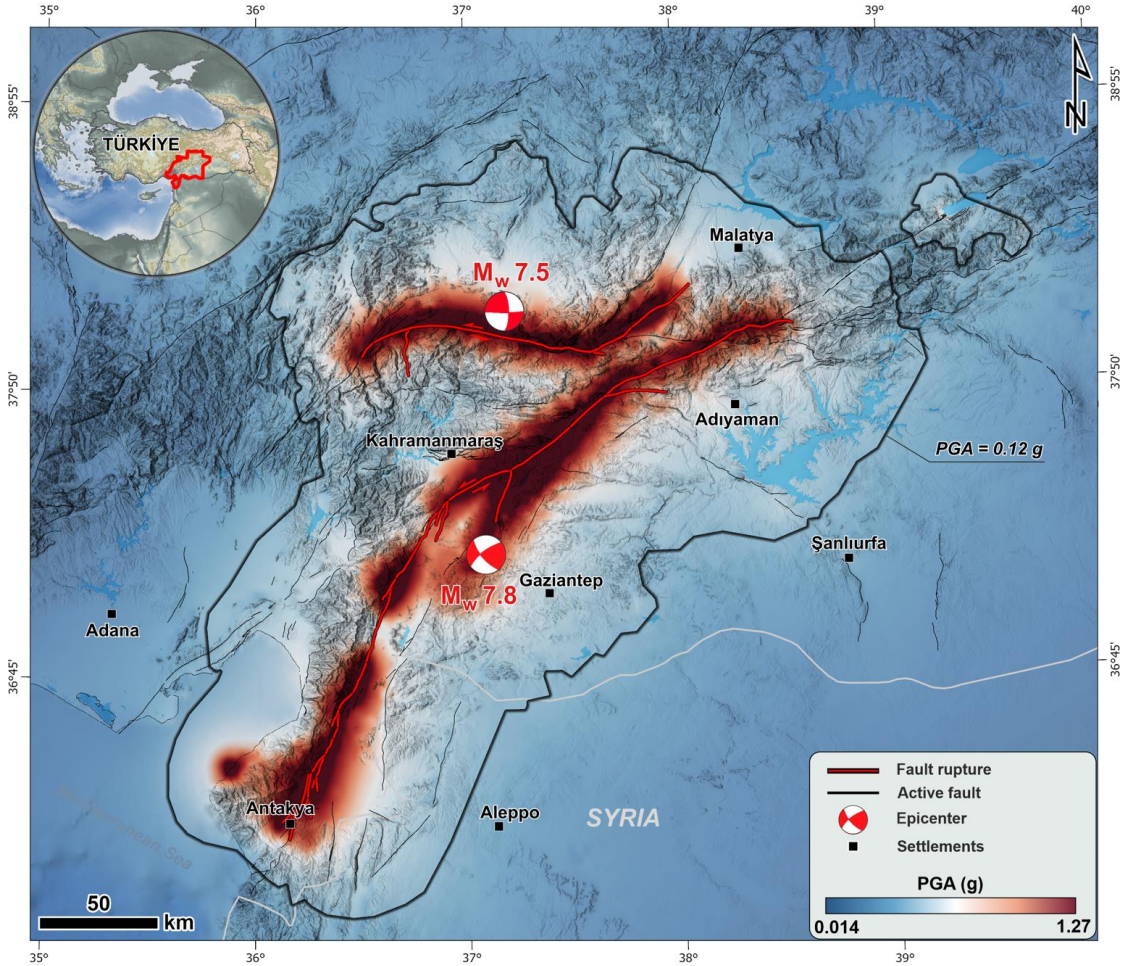

Fig. 1 Seismic source geometry and peak ground acceleration in the 6 February 2023 Türkiye earthquake sequence. Epicentres and surface ruptures for the M_w 7.8 Pazarcık and M_w 7.5 Elbistan earthquakes[47] overlaid on the USGS composite peak ground acceleration (PGA, in g), showing the maximum PGA from all sequence events with $M_w \geq 5.5$[48]. The 0.12 g contour (black) marks the minimum PGA threshold enclosing ≥ 90% of estimated coseismic landslides[49]; white lines show active faults[50].

The sequence affected 11 provinces with a resident population of about 14.01 million (World Bank and Global Facility for Disaster Reduction and Recovery, 2023) and post-disaster assessments identified more than 300,000 buildings classified as collapsed or moderately to heavily damaged (Presidency of the Republic of Türkiye, Strategy and Budget Office, reported in EERI–SSEER, 2025). Settlements such as Kırıkhan (Hatay) and İslahiye (Gaziantep) experienced elevated building collapse and severe damage due to their close proximity to the fault traces[54].

Climatically, the study area lies at the transition between the Mediterranean and continental regimes. Winters are typically cool and wet, whereas summers are hot and dry, with strong spatial variability controlled by elevation and latitude[55]. According to the Köppen–Geiger classification, the region includes several climate types, ranging from cold semi-arid in the northern highlands to warm- and hot-summer Mediterranean climates in the southern lowlands[56]. The rugged topography, dominated by the Taurus and Eastern Anatolian mountains, exerts a major influence on precipitation distribution and runoff patterns. The combination of steep terrain, active tectonics, and climatic variability makes the area highly prone to slope instability.

Preliminary field investigations and satellite-based analyses documented approximately 3,600 and 2,600 coseismic landslides mapped by Görüm et al.[57] and Kocaman et al.[58], respectively. As a result an extensive damage to infrastructure including farmland, railways, highways, and pipelines were reported[59,60]. Also, the earthquakes triggered widespread liquefaction across SE Türkiye and NW Syria, mostly in agricultural non-urban areas along meandering rivers, coastal plains, drained lakes, swamps, and lacustrine basins[61–63]. Post-seismic hydrometeorological events, including an intense atmospheric river about one month after the earthquakes, triggered additional slope failures and floods[64,65].

Methods

Input data

We compiled two landslide inventories, one representing pre-earthquake conditions and the other the coseismic phase, using systematic expert visual interpretation of optical imagery. For the pre-event conditions, we used a 5 m DEM derived from pre-earthquake stereo aerial photographs largely acquired in 2019 by the Turkish General Directorate of Mapping (HGM) (Table 1; Fig. 2a). For the coseismic inventory, we primarily analysed 29,085 high-resolution (0.3 m) post-event aerial photographs covering 66,366 km² collected by HGM between February and September 2023, and complemented these with SPOT-6/7 imagery (1.5 m), Pléiades data (0.5 m) provided by AIRBUS, and MAXAR imagery (0.3 m) from MAXAR Open Data, available for both pre- and post-seismic conditions (Table 1; Fig. 2b).

Table 1 Optical imagery used for mapping the pre-earthquake and coseismic landslide inventories. The table lists the optical image sources and key characteristics used for visual interpretation, including acquisition dates, spatial resolution, and spatial coverage/footprints.

Sources	Resolution (m)	Pre-earthquake imagery			Post-seismic imagery		
		# of images	Total area (km²)	Dates	# of images	Total area (km²)	Dates
Aerial photos	0.3	7,560	43,468	06-09-2016/ 15-08-2020	29,085	69,366	07-02-2023/ 18-09-2023
SPOT-6&7	1.5	19	106,331	03-04-2022/ 20-12-2022	20	64,641	07-02-2023/ 09-03-2023
MAXAR	0.3	18	3,386	01-06-2010/ 26-01-2023	24	20,113	07-02-2023/ 28-02-2023
Pléiades	0.5				13	5,255	08-02-2023/ 01-03-2023

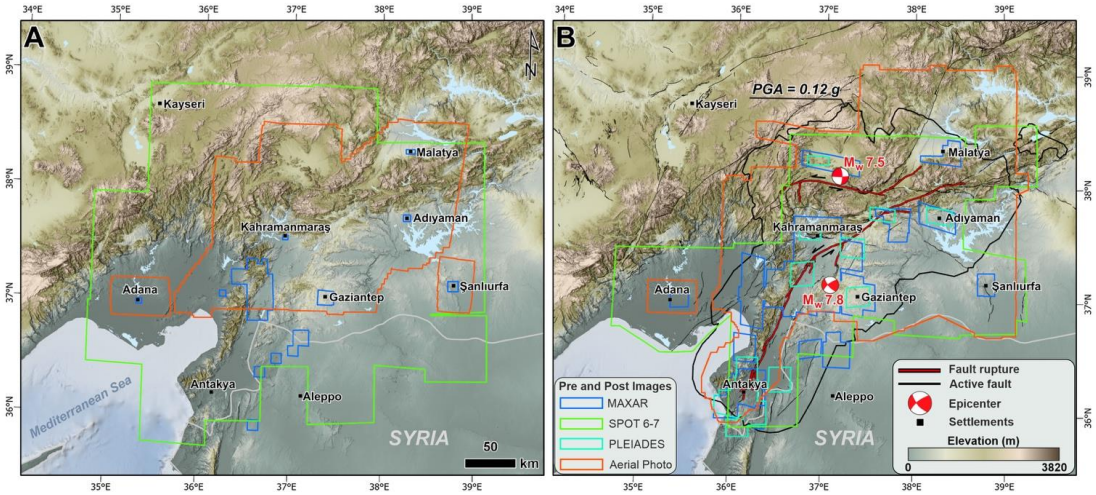

Fig. 2 Spatial footprints of datasets used to compile the pre-earthquake and coseismic inventories. Panels show the areal coverage and image footprints used to map (a) pre-

earthquake landslides and (b) coseismic landslides. Fault ruptures were taken from Goldberg et al.[48]. The 0.12 g PGA contours indicated by black lines were generated from the USGS composite PGA map representing the maximum PGA recorded at each location for all quakes of magnitude 5.5 and larger from the sequence[48].

Mapping pre-seismic landslides

To map pre-earthquake landslides, we systematically examined Red Relief Image Maps (RRIMs, Fig. 3) generated for the whole area. For the generation of RRIMs we used the 5 m DEM, following the method described by Chiba et al.[66]. RRIM is a hillshade-independent, multi-layer visualization that enhances three key geomorphic elements simultaneously: overall slope, convex ridgelines, and concave hollows[67]. The maps were produced by fusing the slope field with the RRIM index I, which is derived from positive openness (O_p) and negative openness (O_n). In this context, openness quantifies the angular exposure of a surface toward the sky (O_p) and toward the ground (O_n), providing a robust discriminator between convex and concave landforms[68]. This approach yields illumination-invariant relief imagery that sharply delineates geomorphic structure (Fig. 3) across the full extent of the study area.

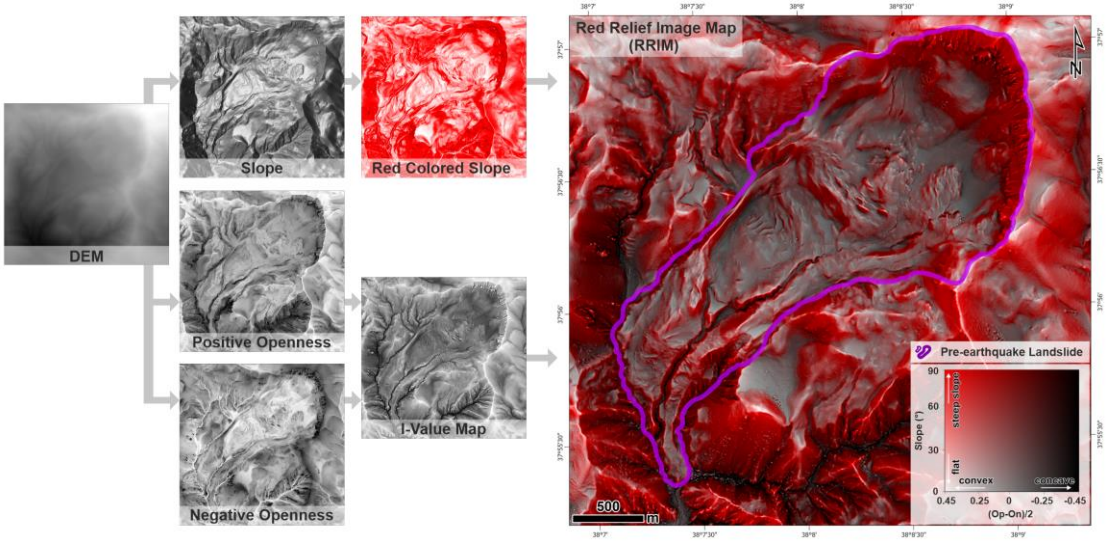

Fig. 3 Example workflow for delineating pre-earthquake landslides using relief-enhanced visualization. Red Relief Image Maps (RRIMs) generated from a 5 m DEM provide illumination-independent relief to support systematic visual interpretation of pre-existing landslide morphology.

Pre-earthquake landslides were mapped as a historical (geomorphological) landslide inventory. Therefore, we could not document the occurrence dates or triggering factors of those landslides. We generated this inventory to simply show the areas historically affected by some landslides before the earthquake. We mapped all landslides as polygons.

Mapping coseismic landslides

We mapped coseismic landslides as single polygons representing the full impacted area (source, path, and deposit), without partitioning source and deposit. As with the pre-earthquake inventory, mapping was based on systematic expert visual interpretation of optical imagery. To isolate coseismic failures, we bracketed the time window with pre- and post-earthquake images (Table 1), excluding features present before the earthquakes and those first appearing after the intense rainfall event roughly one month later[64].

Post-seismic observations were occasionally hindered by snow and cloud cover[57]. In such cases, we extended the acquisition window from images obtained immediately after the

earthquakes (February 2023) to later dates through September 2023, and interpreted multi-temporal stacks jointly rather than in isolation. When a landslide could be confirmed in the earliest available post-event imagery, we delineated its polygon accordingly. Conversely, features that were absent in those early images but appeared only in later scenes were classified as post-seismic landslides and excluded from the coseismic inventory.

We also classified landslides by movement and by material following Varnes[69] and Hungr et al.[70]. Movement classes included fall, slide, flow, lateral spread, and avalanche, with a complex category for multi-mechanism events: slide–flow and slide–avalanche. Material classes included earth, debris, rock, and rock–debris.

Classification of coseismic landslide types

We further classified the coseismic landslides by movement and material, using high-resolution optical imagery, multi-temporal context, and local geomorphic setting as primary decision criteria. For movement, we adopted a seven-class scheme[69,70] comprising avalanche, slide, fall, flow, lateral spread, and two complex classes where more than one mechanism is evident. Fig. 4 provides representative examples and polygons for each class: avalanche (rapid, channelized or unconfined downslope movement; Fig. 4a), slide (coherent displacement along a discernible basal surface; Fig. 4b), fall (near-vertical detachment from cliffs or steep headwalls with talus accumulation; Fig. 4c), flow (internally deforming, often lobate deposits with diffuse margins; Fig. 4d), and lateral spread (predominantly horizontal extension and cracking, typically on low gradients or along riverbanks; Fig. 4e). Complex events were assigned where sequential or coeval mechanisms are evident, for example, slide–flow (a translational or rotational slide transitioning downslope into a deforming flow lobe; Fig. 4f) and slide–avalanche (initial sliding accompanied by high-velocity entrainment and fragmented transport; Fig. 4g). Movement class was determined from planform morphology, runout style, headscarp expression, internal texture, and the evolution observed across the pre- and post-event image stack; we recorded a complex label whenever the imagery indicated mixed kinematics during initiation and transport.

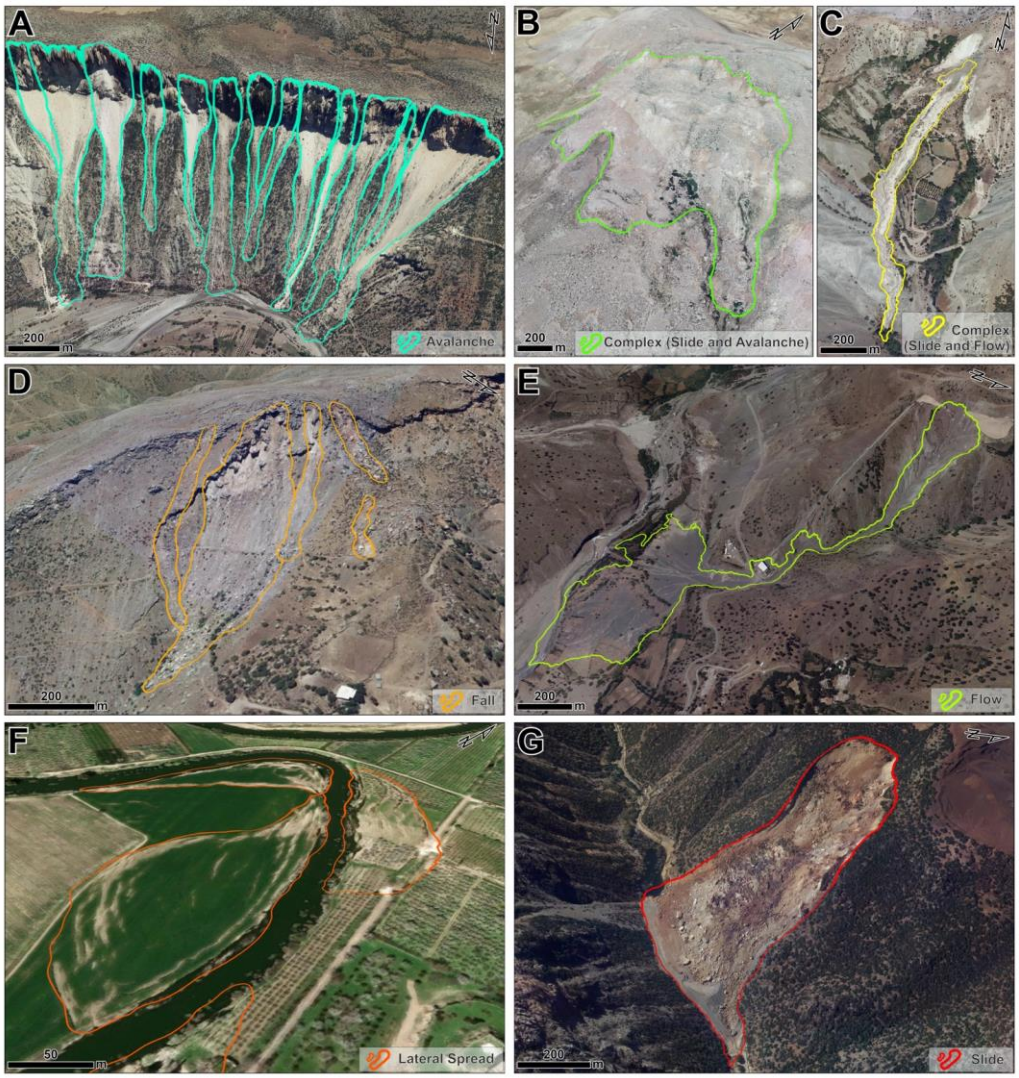

Fig. 4 Representative examples of movement-based landslide classes used in the coseismic inventory. Panels show examples of (a) avalanche, (b) slide, (c) fall, (d) flow, (e) lateral spread, and complex multi-mechanism classes including (f) slide–flow and (g) slide–avalanche.

For material, we distinguished four classes that were mappable from optical imagery at our working resolutions (0.3–1.5 m): earth, debris, rock, and rock–debris. Fig. 5 shows representative polygons for each: earth (fine-grained or soil-dominated surficial cover with smooth, diffuse deposits; Fig. 5a), debris (heterogeneous mixture of soil and coarse fragments, typically with granular textures and leveed margins; Fig. 5b), rock (blocky clasts, angular boulders, and fresh bedrock exposures indicative of rockfalls or rockslides; Fig. 5c), and rock–debris (mixed signatures where coarse blocky material is interbedded or mantled by finer sediment; Fig. 5d). Material class assignments leveraged spectral tone, surface roughness, clast-size expression (where resolvable), proximity to bedrock outcrops, and context such as lithology inferred from mapped geology and terrain position (ridges, cliffs, valley walls). Where image evidence remained ambiguous, we favored the rock–debris mixed category rather than over-specifying end-member classes.

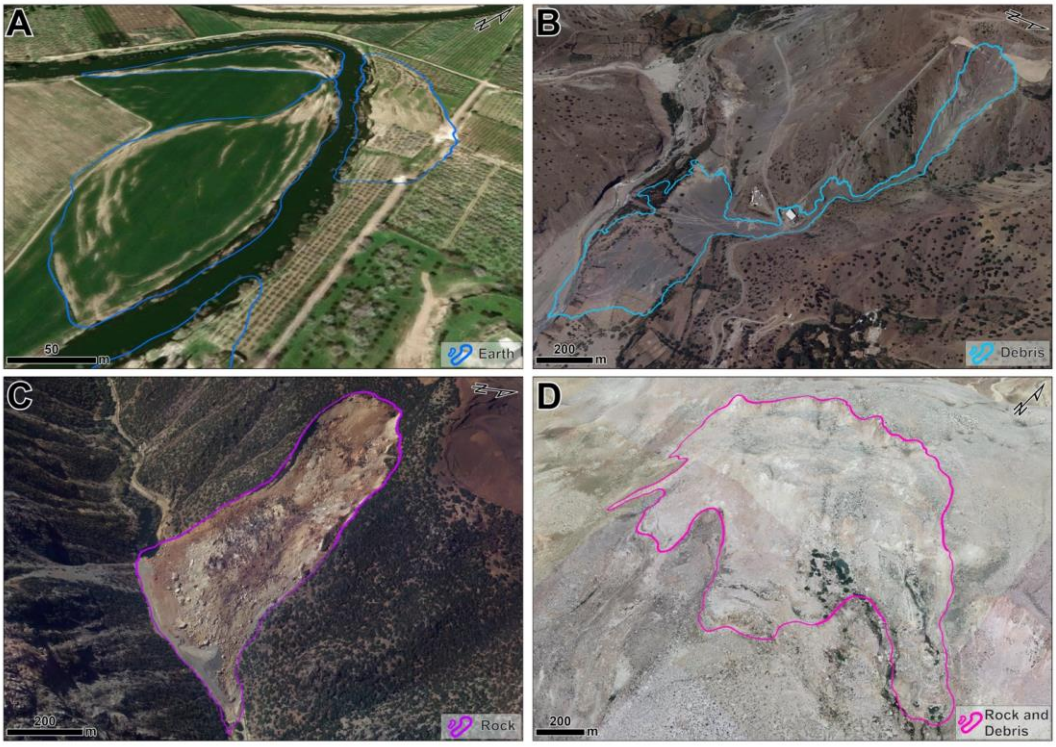

Fig. 5 Representative examples of material-based landslide classes used in the coseismic inventory. Panels show examples of (a) earth, (b) debris, (c) rock, and (d) rock–debris material classes.

Across both taxonomies, polygons represent the entire impacted footprint (source, path, and deposit). Class labels were assigned at the polygon level and reflect the dominant mechanism and material during the coseismic phase captured by our temporal window. We note that some landslides may evolve kinematically through time; in such cases the complex label was applied. Classification confidence is highest where headscarps, transport zones, and deposits are well expressed in multiple post-event images and where pre-event imagery provides a clear baseline; confidence decreases in vegetated terrain, shadowed aspects, or where snow/cloud impeded inspection, and these cases were cross-checked using later clear-sky acquisitions and, where available, field photographs and UAV imagery.

Data Records

This work releases two geospatial data records: (1) a pre-earthquake geomorphic landslide inventory (Fig. 6a) and (2) a coseismic landslide polygon inventory for the same region (Fig 6b) where landslides are classified based on both movement (Fig. 6c) and material (Fig. 6d) types. The records are provided in ESRI Shapefile format for direct use in GIS software, together with a README file describing the contents.

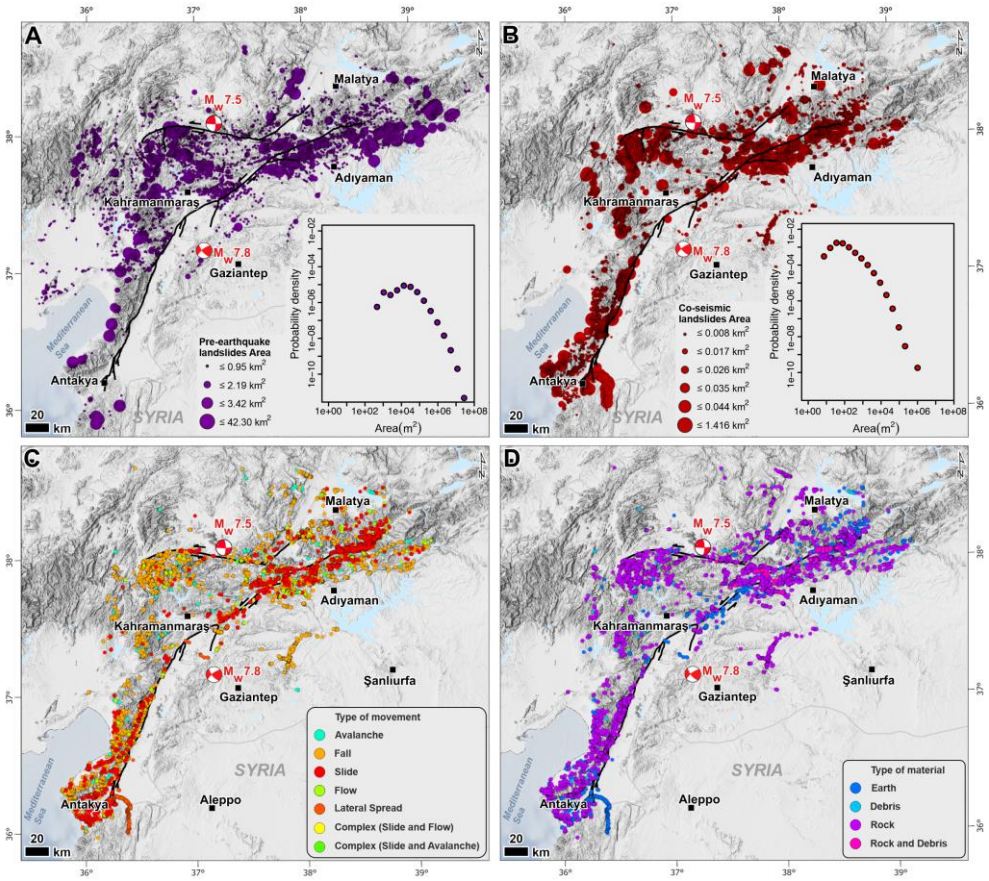

Fig. 6 Regional distribution of pre-earthquake and coseismic landslides and their class attributes. Panels show the spatial distribution of (a) pre-earthquake landslides and (b) coseismic landslides, and classified coseismic landslides by (c) movement type and (d) material type. In panels (a) and (b), circle radius represents landslide area; size classes are binned using standard-deviation thresholds computed separately for each distribution.

Data record 1 and 2 consist of polygon geometries representing mapped coseismic landsldies and pre-earthquake landslide footprints. The record is distributed as an ESRI Shapefile, which comprises multiple component files that must be kept together in the same directory to ensure correct use in GIS environments.

Coordinate reference system. The dataset is provided in a projected coordinate system based on WGS 1984 Transverse Mercator (central meridian = 36°E, scale factor = 1.0, false easting = 500,000 m, false northing = 0 m), using meters as linear units. The underlying geographic coordinate system is WGS 1984 (EPSG:4326).

Data record 1: Coseismic landslide polygon inventory

Archived file set (Shapefile + documentation):

- Coseismic_Landslides_Inventory_2023_EQ_Turkiye.shp (polygon geometries)
- Coseismic_Landslides_Inventory_2023_EQ_Turkiye.dbf (attribute table)
- Coseismic_Landslides_Inventory_2023_EQ_Turkiye.prj (projection definition)
- Coseismic_Landslides_Inventory_2023_EQ_Turkiye.cpg (character encoding)
- Shapefile index and spatial index files generated during export (e.g., .shx and, where present, .sbn/.sbx)
- README.txt (dataset description and usage notes)

Attribute table definitions. Each polygon corresponds to one mapped landslide footprint and is associated with the following attributes:

- **FID**: Feature identifier automatically generated by GIS software; not intended as a stable identifier for analysis.
- **Shape**: Polygon geometry representing the landslide footprint.
- **Id**: Unique identifier assigned to each landslide polygon (recommended stable key for analysis).
- **Type**: Landslide movement class label (categorical; *avalanche, slide, fall, flow, lateral spread,* and *complex* types).
- **Area**: Landslide polygon area (m^2), calculated from the polygon geometry in the projected coordinate system.
- **Mat_Type**: Material type (categorical; *earth, debris, rock,* and *rock–debris*).
- **Mov_Type**: Movement type (categorical; e.g., *avalanche, fall, slide, flow, lateral spread,* and *complex*).

Data record 2: Pre-earthquake geomorphic inventory

Archived file set (Shapefile + documentation):

- Preseismic_Landslides_Inventory_2023_EQ_Turkiye.shp
- Preseismic_Landslides_Inventory_2023_EQ_Turkiye.dbf
- Preseismic_Landslides_Inventory_2023_EQ_Turkiye.shx
- Preseismic_Landslides_Inventory_2023_EQ_Turkiye.prj
- Preseismic_Landslides_Inventory_2023_EQ_Turkiye.cpg
- README.txt (dataset description and usage notes)

Attribute table definitions. Each polygon corresponds to one mapped landslide footprint and is associated with the following attributes:

- **FID**: Feature identifier automatically generated by GIS software; not intended as a stable identifier for analysis.
- **Shape**: Polygon geometry representing the landslide footprint.
- **Id**: Unique identifier assigned to each landslide polygon (recommended stable key for analysis).
- **Area_m2**: Landslide polygon area (m^2), calculated from the polygon geometry in the projected coordinate system.
- **Area_km2**: Landslide polygon area (km^2), calculated from the polygon geometry in the projected coordinate system.

Technical Validation

Three factors impeded mapping in some scenes: cloud cover, snow cover and differentiating post-seismic landslides. To mitigate these issues, we examined multi-temporal image stacks of the same locations.

Snow cover obscured several coseismic landslides in scenes acquired shortly after the earthquake doublet (in February 2023). However, we could often identify failures by comparing pre- and post-event imagery despite snow (Fig. 7a, b), reliable boundary delineation required scenes obtained after snowmelt (Fig. 7c, d). We applied the same multi-temporal strategy to areas masked by cloud cover in early acquisitions (Fig. 8).

Fig. 7 Example of addressing snow-related visibility limitations during landslide mapping. Panels show (a) pre-earthquake Google Earth imagery acquired on 6 April 2022; (b) post-earthquake aerial imagery acquired on 10 February 2023 where snow cover hinders interpretation; (c) post-earthquake imagery acquired on 11 July 2023 after snowmelt; and (d) a zoomed view of the same area illustrating the landslide boundary mapped with improved visibility.

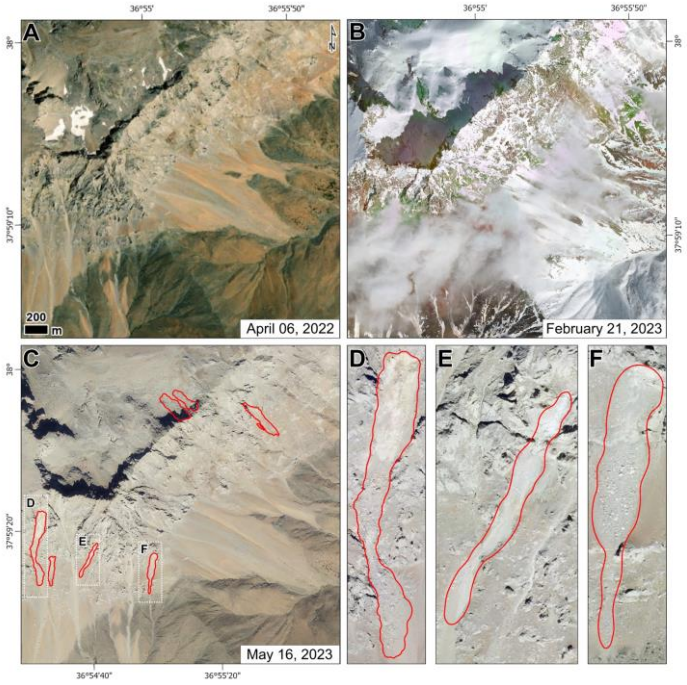

Fig. 8 Example of addressing cloud-related visibility limitations during landslide mapping. Panels show (a) pre-earthquake Google Earth imagery acquired on 6 April 2022; (b) post-earthquake aerial imagery acquired on 21 February 2023 where cloud cover hinders interpretation; (c) post-earthquake imagery acquired on 16 May 2023 under clear conditions; and (d–f) zoomed views of the same area illustrating landslide boundaries mapped reliably once cloud obscuration is removed.

Separating pre- and post-seismic features posed an additional challenge. Using multi-temporal imagery, we removed pre-existing landslides from the coseismic inventory and also screened out post-seismic landslides associated with the extreme rainfall event about one month after the doublet (Fig. 9), which was exacerbated by an atmospheric river[64]. These rainfall-triggered landslides were excluded from the coseismic inventory, but they were not mapped systematically.

We conducted two targeted field campaigns to ground-truth landslides mapped from remote sensing. Following the earthquakes, field teams visited priority sites in March and June 2023 where additional observations were needed beyond image interpretation. During these surveys, we collected close-range imagery using a DJI Mavic 2 Pro UAV to document slope morphology and support validation of mapped landslide footprints and class labels. Fig. 10 provides representative UAV examples of landslide types observed in the field. The examples were selected to span sites distributed from south to north across the surveyed region.

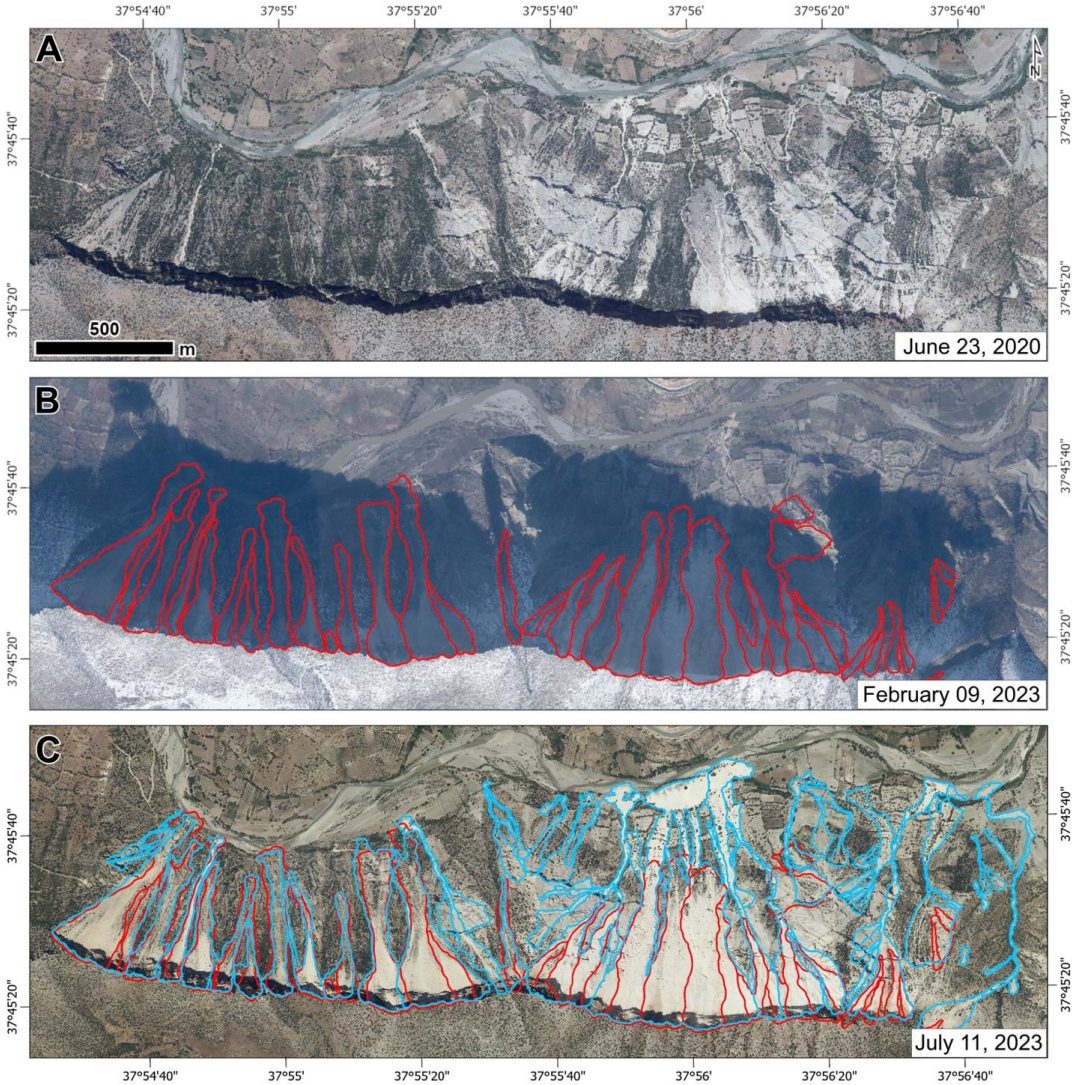

Fig. 9 Example of separating post-seismic rainfall-triggered landslides from coseismic failures using multi-temporal imagery. Panels show (a) pre-earthquake aerial imagery acquired on 23 June 2020; (b) post-earthquake aerial imagery acquired on 9 February 2023 with coseismic landslides delineated in red; and (c) post-earthquake imagery acquired after the 15 March 2023 rainfall event, highlighting additional rainfall-triggered landslides mapped in cyan.

Fig. 10 Drone imagery examples used for validation of mapped landslides. Panels show representative UAV views of mapped failures, including (a) avalanche, (b) complex slide–avalanche, (c) complex slide–flow, (d) fall, (e) flow, (f) lateral spread, and (g) slide. The locations of the UAV image sites are shown in Panel (f).

Code Availability

No custom code was used to generate or process the datasets. All mapping, digitization, and attribute editing were performed using Esri ArcGIS Pro (version 3.6) using standard, built-in geoprocessing and editing tools.

Data Availability

The dataset will become available upon publication.

Acknowledgements

This study was supported by the NATO Science for Peace and Security Program (SPS Grant Number G6190) and the Scientific and Technological Research Council of Turkey (TUBITAK) under grant number 123Y212. We would like to express our sincere gratitude to the Ministry of Defence, Directorate General for Mapping (HGM), for their invaluable support throughout all stages of this study. Special thanks are extended to Major General Osman Alp, Colonel

Orhan Fırat, and Colonel Dr. Abdullah Değer, as well as the entire HGM team, for their dedicated efforts in conducting repeated aerial surveys and collecting high-resolution data following the earthquake, which significantly contributed to post-seismic research. H.T. acknowledges support from the European Space Agency, AMHEI project, 4000144311/24/I-KE.

Author contributions

A.Y. Conceptualization; data curation; investigation; formal analysis; visualization; writing—original draft; writing—review & editing; resources.
H.T. Conceptualization; data curation; investigation; formal analysis; visualization; writing—original draft; writing—review & editing; funding acquisition.
F.K. Visualization; resources.
M.L.S. Data curation; investigation.
T.G. Conceptualization; data curation; investigation; formal analysis; visualization; writing—original draft; writing—review & editing; funding acquisition.

Competing interests

The authors declare that they have no conflict of interest.

References

1. Gorum, T. *et al.* Distribution pattern of earthquake-induced landslides triggered by the 12 May 2008 Wenchuan earthquake. *Geomorphology* **133**, 152–167 (2011).
2. Massey, C. *et al.* Landslides triggered by the 14 November 2016 Mw 7.8 Kaikōura earthquake, New Zealand. *Bulletin of the Seismological Society of America* **108**, 1630–1648 (2018).
3. Baum, R. L. & Godt, J. W. Early warning of rainfall-induced shallow landslides and debris flows in the USA. *Landslides* **7**, 259–272 (2010).
4. Crosta, G. B. & Frattini, P. Distributed modelling of shallow landslides triggered by intense rainfall. *Nat. Hazards Earth Syst. Sci.* **3**, 81–93 (2003).
5. Aslan, H. *et al.* Atmospheric rivers catalyze snowmelt and contribute to chains of landslides. *CATENA* **260**, 109503 (2025).
6. Cardinali, M., Ardizzone, F., Galli, M., Guzzetti, F. & Reichenbach, P. Landslides triggered by rapid snow melting: the December 1996–January 1997 event in Central Italy. in 439–448 (Bios Publisher, Cosenza, 2000).
7. Dille, A. *et al.* Acceleration of a large deep-seated tropical landslide due to urbanization feedbacks. *Nat. Geosci.* **15**, 1048–1055 (2022).

8. Froude, M. J. & Petley, D. N. Global fatal landslide occurrence from 2004 to 2016. *Natural Hazards and Earth System Sciences* **18**, 2161–2181 (2018).
9. Guzzetti, F. *et al.* Landslide inventory maps: New tools for an old problem. *Earth-Science Reviews* **112**, 42–66 (2012).
10. Malamud, B. D., Turcotte, D. L., Guzzetti, F. & Reichenbach, P. Landslide inventories and their statistical properties. *Earth Surface Processes and Landforms* **29**, 687–711 (2004).
11. Fan, X. *et al.* Earthquake-Induced Chains of Geologic Hazards: Patterns, Mechanisms, and Impacts. *Reviews of Geophysics* **57**, (2019).
12. Korup, O., Densmore, A. L. & Schlunegger, F. The role of landslides in mountain range evolution. *Geomorphology* **120**, 77–90 (2010).
13. Wang, J. *et al.* Long-term patterns of hillslope erosion by earthquake-induced landslides shape mountain landscapes. *Sci. Adv.* **6**, eaaz6446 (2020).
14. Fan, X. *et al.* Deep learning can predict global earthquake-triggered landslides. *National Science Review* **12**, nwaf179 (2025).
15. Nowicki Jessee, M. A. *et al.* A global empirical model for near-real-time assessment of seismically induced landslides. *Journal of Geophysical Research: Earth Surface* **123**, 1835–1859 (2018).
16. Allstadt, K. E. *et al.* The US Geological Survey ground failure product: Near-real-time estimates of earthquake-triggered landslides and liquefaction. *Earthquake Spectra* **38**, 5–36 (2022).
17. Tanyaş, H. *et al.* Presentation and Analysis of a Worldwide Database of Earthquake-Induced Landslide Inventories. *Journal of Geophysical Research: Earth Surface* https://doi.org/10.1002/2017JF004236 (2017) doi:10.1002/2017JF004236.
18. Schmitt, R. G. *et al. An Open Repository of Earthquake-Triggered Ground-Failure Inventories*. 26–26 (2017) doi:10.3133/ds1064.

19. Harp, E. L., Keefer, D. K., Sato, H. P. & Yagi, H. Landslide inventories: The essential part of seismic landslide hazard analyses. *Engineering Geology* **122**, 9–21 (2011).
20. Fang, C. *et al.* A globally distributed dataset of coseismic landslide mapping via multi-source high-resolution remote sensing images. *Earth Syst. Sci. Data* **16**, 4817–4842 (2024).
21. Nava, L., Monserrat, O. & Catani, F. Improving Landslide Detection on SAR Data Through Deep Learning. *IEEE Geosci. Remote Sensing Lett.* **19**, 1–5 (2022).
22. GSI (Geospatial Information Authority of Japan). *1:25,000 Damage Map of the Mid Niigata Prefecture Earthquake in 2004: 3 Sheets*. (2005).
23. Roback, K. *et al.* The size, distribution, and mobility of landslides caused by the 2015 Mw7.8 Gorkha earthquake, Nepal. *Geomorphology* **301**, 121–138 (2018).
24. Yagi, H., Yamasaki, T. & Masahiro, A. GIS analysis on geomorphological features and soil mechanical implication of landslides caused by 2004 Niigata Chuetsu earthquake. *Journal of the Japan Landslide Society* **43**, 294–306 (2007).
25. Sepúlveda, S. A., Serey, A., Lara, M., Pavez, A. & Rebolledo, S. Landslides induced by the April 2007 Aysén Fjord earthquake, Chilean Patagonia. *Landslides* **7**, 483–492 (2010).
26. Yagi, H., Sato, G., Higaki, D., Yamamoto, M. & Yamasaki, T. Distribution and characteristics of landslides induced by the Iwate-Miyagi Nairiku Earthquake in 2008 in Tohoku District, Northeast Japan. *Landslides* **6**, 335–344 (2009).
27. Wartman, J., Dunham, L., Tiwari, B. & Pradel, D. Landslides in eastern Honshu induced by the 2011 Off the Pacific Coast of Tohoku earthquake. *Bulletin of the Seismological Society of America* **103**, 1503–1521 (2013).
28. Fan, X. *et al.* Spatio-temporal evolution of mass wasting after the 2008 Mw 7.9 Wenchuan earthquake revealed by a detailed multi-temporal inventory. *Landslides* **15**, 2325–2341 (2018).

29. Kincey, M. *et al.* Evolution of coseismic and post-seismic landsliding after the 2015 Mw 7.8 Gorkha earthquake, Nepal. *Earth and Space Science Open Archive ESSOAr* https://doi.org/10.1002/essoar.10505237.1 (2020) doi:10.1002/essoar.10505237.1.
30. Tanyaş, H. *et al.* A closer look at factors governing landslide recovery time in post-seismic periods. *Geomorphology* **391**, 107912–107912 (2021).
31. Samia, J. *et al.* Do landslides follow landslides? Insights in path dependency from a multi-temporal landslide inventory. *Landslides* **14**, 547–558 (2017).
32. Gorum, T. *et al.* Complex rupture mechanism and topography control symmetry of mass-wasting pattern, 2010 Haiti earthquake. *Geomorphology* **184**, 127–138 (2013).
33. Arpat, E. & Şaroğlu, F. Doğu Anadolu Fayı ile ilgili bazı gözlem ve düşünceler. *MTA dergisi* **78**, 44–50 (1972).
34. Duman, T. Y. & Emre, Ö. The East Anatolian Fault: geometry, segmentation and jog characteristics. *Geological Society, London, Special Publications* **372**, 495–529 (2013).
35. Reilinger, R. *et al.* GPS constraints on continental deformation in the Africa-Arabia-Eurasia continental collision zone and implications for the dynamics of plate interactions. *Journal of Geophysical Research: Solid Earth* **111**, (2006).
36. Herece, E. Doğu Anadolu Fayı (DAF) Atlası. in (2008).
37. Şengör, A. M. C. & Yazıcı, M. The aetiology of the neotectonic evolution of Turkey. *Mediterranean Geoscience Reviews* **2**, 327–339 (2020).
38. Aktug, B. *et al.* Slip rates and seismic potential on the East Anatolian Fault System using an improved GPS velocity field. *Journal of Geodynamics* **94–95**, 1–12 (2016).
39. Karabacak, V. *et al.* The 2023 Pazarcık (Kahramanmaraş, Türkiye) earthquake (Mw 7.7): implications for surface rupture dynamics along the East Anatolian Fault Zone. *Journal of the Geological Society* **180**, jgs2023-020 (2023).

40. Kurcer, A. *et al. 06 Şubat 2023 Pazarcık (Kahramanmaraş) Depremi (Mw 7,8) Saha Gözlemleri ve Değerlendirmeler. MTA Genel Müdürlüğü, Rapor No: 14138, 187 s., Ankara (In Turkish)*. (2023).
41. Provost, F. *et al.* High-resolution co-seismic fault offsets of the 2023 Türkiye earthquake ruptures using satellite imagery. *Scientific Reports* **14**, 6834–6834 (2024).
42. Abdelmeguid, M. *et al.* Dynamics of episodic supershear in the 2023 M7.8 Kahramanmaraş/Pazarcik earthquake, revealed by near-field records and computational modeling. *Communications Earth & Environment* **4**, 456–456 (2023).
43. Li, S. *et al.* Source Model of the 2023 Turkey Earthquake Sequence Imaged by Sentinel-1 and GPS Measurements: Implications for Heterogeneous Fault Behavior along the East Anatolian Fault Zone. *Remote Sensing* **15**, (2023).
44. Mai, P. M. *et al.* The Destructive Earthquake Doublet of 6 February 2023 in South-Central Türkiye and Northwestern Syria: Initial Observations and Analyses. *The Seismic Record* **3**, 105–115 (2023).
45. Okuwaki, R., Yuji, Y., Taymaz, T. & Hicks, S. P. Multi-scale rupture growth with alternating directions in a complex fault network during the 2023 south-eastern Türkiye and Syria earthquake doublet. (2023).
46. Liu, C. *et al.* Complex multi-fault rupture and triggering during the 2023 earthquake doublet in southeastern Türkiye. *Nature Communications* **14**, 5564–5564 (2023).
47. Reitman, N. G. *et al.* Preliminary fault rupture mapping of the 2023 M7. 8 and M7. 5 Türkiye Earthquakes. *USGS: Reston, VA, USA* (2023).
48. Goldberg, D. E. *et al.* Rapid Characterization of the February 2023 Kahramanmaraş, Türkiye, Earthquake Sequence. *The Seismic Record* **3**, 156–167 (2023).
49. Tanyaş, H. & Lombardo, L. Variation in landslide-affected area under the control of ground motion and topography. *Engineering Geology* **260**, (2019).
50. Emre, Ö. *et al.* Açıklamalı Türkiye Diri Fay Haritası. *Ölçek* **1**, 0–0 (2013).

51. World Bank & Global Facility for Disaster Reduction and Recovery (GFDRR). *Global Rapid Post-Disaster Damage Estimation (GRADE) Report: February 2023 Kahramanmaraş, Türkiye Earthquakes*. https://openknowledge.worldbank.org/entities/publication/ba591968-fbfd-4443-b859-2bc30906f6fa (2023).
52. Presidency of the Republic of Türkiye, Strategy and Budget Office (SBO). *Türkiye Earthquakes Recovery and Reconstruction Assessment (TERRA)*. https://www.sbb.gov.tr/wp-content/uploads/2023/03/Turkiye-Recovery-and-Reconstruction-Assessment.pdf (2023).
53. EERI Learning from Earthquakes (LFE) & StEER–SSEER. *2023 Kahramanmaraş, Türkiye Earthquake Sequence: Observations of Recovery 20 Months After*. https://learningfromearthquakes.org/wp-content/uploads/EERI-SSEER-Reconnaissance-Report-2023-Turkey-Earthquakes-Recovery-20-Months-After.pdf (2025).
54. Yilmaz, Z. *et al.* Regional Building Damage Survey Data on the 2023 Kahramanmaraş, Türkiye, Earthquakes. *ASCE OPEN: Multidiscip. J. Civ. Eng.* **2**, 04024009 (2024).
55. Lionello, P. *et al.* The Mediterranean climate: An overview of the main characteristics and issues. in *Mediterranean* (eds Lionello, P., Malanotte-Rizzoli, P. & Boscolo, R. B. T.-D. in E. and E. S.) vol. 4 1–26 (Elsevier, 2006).
56. Peel, M. C., Finlayson, B. L. & McMahon, T. A. Updated world map of the Köppen-Geiger climate classification. *Hydrol. Earth Syst. Sci.* **11**, 1633–1644 (2007).
57. Görüm, T. *et al.* Preliminary documentation of coseismic ground failure triggered by the February 6, 2023 Türkiye earthquake sequence. *Engineering Geology* **327**, 107315–107315 (2023).
58. Kocaman, S. *et al.* Landslides triggered by the 6 February 2023 Kahramanmaraş earthquakes (Türkiye). *Turkish Journal of Earth Sciences* **34**, 47–67 (2025).

59. Unal, E. O., Kocaman, S. & Gokceoglu, C. Impact assessment of geohazards triggered by 6 February 2023 Kahramanmaras Earthquakes (Mw 7.7 and Mw 7.6) on the natural gas pipelines. *Engineering Geology* **334**, 107508 (2024).
60. Yan, K. *et al.* Preliminary report of field reconnaissance on the 6 February 2023 Kahramanmaras Earthquakes in Türkiye. *Geoenviron Disasters* **11**, 11, s40677-024-00272–x (2024).
61. Cetin, K. O., Soylemez, B., Guzel, H. & Cakir, E. Soil liquefaction sites following the February 6, 2023, Kahramanmaraş-Türkiye earthquake sequence. *Bull Earthquake Eng* **23**, 921–944 (2025).
62. Taftsoglou, M., Valkaniotis, S., Papathanassiou, G. & Karantanellis, E. Satellite Imagery for Rapid Detection of Liquefaction Surface Manifestations: The Case Study of Türkiye–Syria 2023 Earthquakes. *Remote Sensing* **15**, 4190 (2023).
63. Ulusay, R., Aydan, Ö. & Kumsar, H. Ground liquefaction caused by 6 February 2023 Kahramanmaraş earthquakes of Türkiye and some assessments on its extent and impacts on built environment. *Bull Eng Geol Environ* **83**, 447 (2024).
64. Görüm, T. *et al.* The 2023 Türkiye-Syria earthquake disaster was exacerbated by an atmospheric river. *Communications Earth & Environment* **6**, 151–151 (2025).
65. Jimenez, H. N. *et al.* Modeling the combined effects of the 2023 Türkiye-Syria Earthquake and an Atmospheric River event on landslide hazard. Preprint at https://doi.org/10.5194/egusphere-2025-3011 (2025).
66. Chiba, T., Kaneta, S. & Suzuki, Y. Red relief image map: new visualization method for three dimensional data. *The international archives of the photogrammetry, remote sensing and spatial information sciences* **37**, 1071–1076 (2008).
67. Lin, Z., Kaneda, H., Mukoyama, S., Asada, N. & Chiba, T. Detection of subtle tectonic–geomorphic features in densely forested mountains by very high-resolution airborne LiDAR survey. *Geomorphology* **182**, 104–115 (2013).

68. Yokoyama, R., Shirasawa, M. & Pike, R. J. Visualizing topography by openness: A new application of image processing to digital elevation models. *Photogrammetric engineering and remote sensing* **68**, 257–266 (2002).
69. Varnes, D. Slope Movement Types and Processes. *Special report* **176**, 11–33 (1978).
70. Hungr, O., Leroueil, S. & Picarelli, L. The Varnes classification of landslide types, an update. *Landslides* **11**, 167–194 (2014).